V European Conference on Computational Fluid Dynamics
ECCOMAS CFD 2010
J. C. F. Pereira and A. Sequeira (Eds)
Lisbon, Portugal,14-17 June 2010

TOWARDS HIGH-FIDELITY INDUSTRIAL CFD

Frédéric Chalot* **and Pierre-Elie Normand†**

*Dassault Aviation
78, quai Marcel Dassault – Cedex 300 – 92552 Saint-Cloud Cedex – France
e-mail: frederic.chalot@dassault-aviation.com

†Université de Bordeaux
341, cours de la Libération – 33405 Talence – France
e-mail: pierre-elie.normand@external.dassault-aviation.com

Key words: higher-order stabilized finite elements, compressible Navier-Stokes

Abstract. *This paper describes the extension of Dassault Aviation's stabilized finite element industrial Navier-Stokes code to higher-order elements. The high-order approach is carefully assessed using inviscid subsonic and transonic, laminar, and high Reynolds number turbulent flows. First results on a full aircraft configuration are presented.*

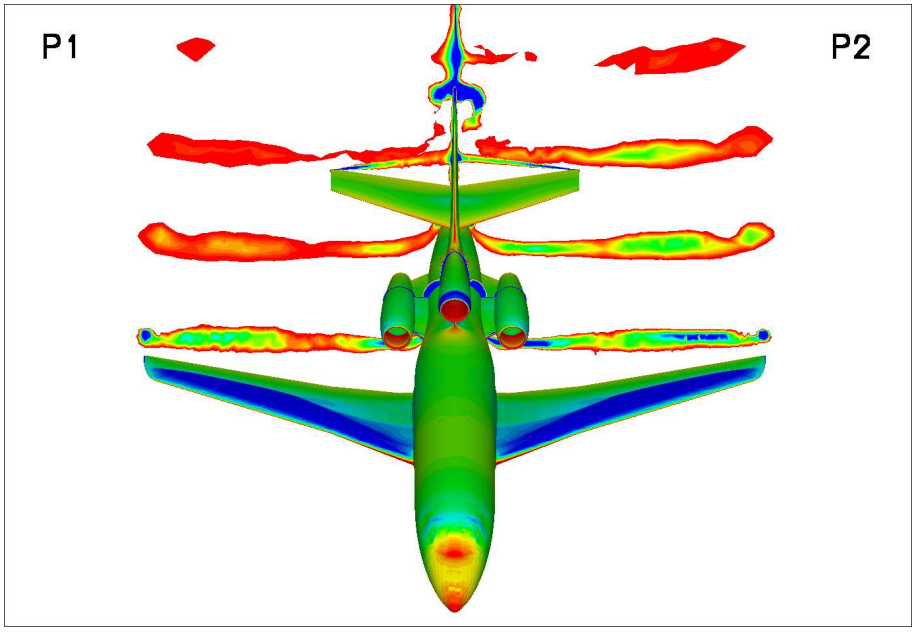

Figure 1: Falcon 900EX: $M = 0.80$, $\alpha = 2.0°$, $Re = 14,500,000$. Pressure contours on the aircraft surface, entropy in the wake; linear (left) and quadratic elements (right) on the same 19,905,887-node mesh.

1 INTRODUCTION

The European project **ADIGMA** (Adaptive Higher-Order Variational Methods for Aerodynamic Application in Industry) (see [1] and `http://www.dlr.de/as/`) proposed a framework to address many of the accuracy and cost issues of current industrial CFD codes. The different partners have put together innovative higher-order methods which will constitute key ingredients for the next generation of industrial flow solvers. The participation of Dassault Aviation focused on higher-order stabilized finite elements for its industrial Navier-Stokes code Aether.

Although Dassault Aviation started from the beginning with unstructured meshes and a Navier-Stokes code based on a finite element formulation, the claim that finite elements can fairly effortlessly and in a straightforward manner go high in order was never fully exploited. We currently still use for all Navier-Stokes calculations linear elements which yield second-order accuracy [6, 10, 11]. A single but successful attempt was made to compute the flow past a supersonic ramp [3] using quadratic elements.

In this paper, higher-order (3^{rd} and 4^{th} order) finite elements in the SUPG/Galerkin-least squares framework are revisited. We present results showing the balance between the resulting improved accuracy and the potentially reduced robustness. Mesh generation aspects are treated and especially the issue of highly-stretched curved elements close to the wall boundary of Navier-Stokes meshes. The high-order approach is carefully assessed using subsonic and transonic inviscid flows, laminar flows, and high Reynolds number turbulent flows. Industrial aspects towards complex 3-D geometries are discussed. First higher-order results on a full aircraft configuration are presented.

2 HIGHER-ORDER STABILIZED FINITE ELEMENT SCHEMES FOR THE RANS EQUATIONS

We present our numerical method in the following sections and highlight the adjustments required by higher-order elements.

2.1 General description of our flow solver

Dassault Aviation's Navier-Stokes code, called `AETHER`, uses a finite element approach, based on a symmetric form of the equations written in terms of entropy variables. The advantages of this change of variables are numerous: in addition to the strong mathematical and numerical coherence they provide (dimensionally correct dot product, symmetric operators with positivity properties, efficient preconditioning), entropy variables yield further improvements over the usual conservation variables, in particular in the context of chemically reacting flows (see [5, 6]).

The code can handle the unstructured mixture of numerous types of elements (triangles and quadrilaterals in 2-D; tetrahedra, bricks, and prisms in 3-D). In practice mostly linear triangular and tetrahedral meshes are used.

Different one- and two-equation Reynolds-averaged turbulence models are available:

Spalart-Allmaras, K-ε, K-ω, K-ℓ, K-KL... These models are either integrated down to the wall, use a two-layer approach with a low-Reynolds modelization of the near wall region, or adopt a wall function treatment of the boundary layer. More advanced RANS models, such as EARSM and RSM, and extensions to LES and DES are also available (see [8], [9], and [11]).

Convergence to steady state of the compressible Navier Stokes equations is achieved through a fully-implicit iterative time-marching procedure based on the GMRES algorithm with nodal block-diagonal or incomplete LDU preconditioning (see [16]).

The code has been successfully ported on many computer architectures. It is fully vectorized and parallelized for shared or distributed memory machines using the MPI message passing library (IBM SP2 Series, IBM Blue Gene, Itanium II- and Xeon-based Bull NovaScale) or native parallelization directives (NEC SX-4) (see [7]).

2.2 The symmetric Navier-Stokes equations

As a starting point, we consider the compressible Navier-stokes equations written in conservative form:

$$\boldsymbol{U}_{,t} + \boldsymbol{F}^{\text{adv}}_{i,i} = \boldsymbol{F}^{\text{diff}}_{i,i} \tag{1}$$

where $\boldsymbol{U}$ is the vector of conservative variables; $\boldsymbol{F}^{\text{adv}}_i$ and $\boldsymbol{F}^{\text{diff}}_i$ are, respectively, the advective and the diffusive fluxes in the i^{th}-direction. Inferior commas denote partial differentiation and repeated indices indicate summation.

Equation (1) can be rewritten in quasi-linear form:

$$\boldsymbol{U}_{,t} + \boldsymbol{A}_i \boldsymbol{U}_{,i} = (\boldsymbol{K}_{ij}\boldsymbol{U}_{,j})_{,i} \tag{2}$$

where $\boldsymbol{A}_i = \boldsymbol{F}^{\text{adv}}_{i,\boldsymbol{U}}$ is the i^{th} advective Jacobian matrix, and $\boldsymbol{K} = [\boldsymbol{K}_{ij}]$ is the diffusivity matrix, defined by $\boldsymbol{F}^{\text{diff}}_i = \boldsymbol{K}_{ij}\boldsymbol{U}_{,j}$. The $\boldsymbol{A}_i$'s and $\boldsymbol{K}$ do not possess any particular property of symmetry or positiveness.

We now introduce a new set of variables,

$$\boldsymbol{V}^T = \frac{\partial \mathcal{H}}{\partial \boldsymbol{U}}$$

where $\mathcal{H}$ is the generalized entropy function given by

$$\mathcal{H} = \mathcal{H}(\boldsymbol{U}) = -\rho s$$

and s is the thermodynamic entropy per unit mass. Under the change of variables $\boldsymbol{U} \mapsto \boldsymbol{V}$, (2) becomes:

$$\widetilde{\boldsymbol{A}}_0 \boldsymbol{V}_{,t} + \widetilde{\boldsymbol{A}}_i \boldsymbol{V}_{,i} = (\widetilde{\boldsymbol{K}}_{ij}\boldsymbol{V}_{,j})_{,i} \tag{3}$$

where

$$\begin{aligned} \widetilde{\boldsymbol{A}}_0 &= \boldsymbol{U}_{,\boldsymbol{V}} \\ \widetilde{\boldsymbol{A}}_i &= \boldsymbol{A}_i \widetilde{\boldsymbol{A}}_0 \\ \widetilde{\boldsymbol{K}}_{ij} &= \boldsymbol{K}_{ij} \widetilde{\boldsymbol{A}}_0. \end{aligned}$$

The Riemannian metric tensor $\widetilde{\boldsymbol{A}}_0$ is symmetric positive-definite; the $\widetilde{\boldsymbol{A}}_i$'s are symmetric; and $\widetilde{\boldsymbol{K}} = [\widetilde{\boldsymbol{K}}_{ij}]$ is symmetric positive-semidefinite. In view of these properties, (3) is referred to as a symmetric advective-diffusive system.

For a general divariant gas, the vector of so-called (physical) entropy variables, $\boldsymbol{V}$, reads

$$\boldsymbol{V} = \frac{1}{T} \left\{ \begin{array}{c} \mu - |\boldsymbol{u}|^2/2 \\ \boldsymbol{u} \\ -1 \end{array} \right\}$$

where $\mu = e + pv - Ts$ is the chemical potential per unit mass; $v = 1/\rho$ is the specific volume. More complex equations of state are treated in [4]. We would like to stress the formal similarity between the conservation variables $\boldsymbol{U}$ and the entropy variables $\boldsymbol{V}$, which can be made more apparent if we write the conservation variables in the following form:

$$\boldsymbol{U} = \frac{1}{v} \left\{ \begin{array}{c} 1 \\ \boldsymbol{u} \\ e + |\boldsymbol{u}|^2/2 \end{array} \right\}$$

where $v = 1/\rho$ is the specific volume.

Taking the dot product of (3) with the vector $\boldsymbol{V}$ yields the Clausius-Duhem inequality, which constitutes the basic nonlinear stability condition for the solutions of (3). This fundamental property is inherited by appropriately defined finite element methods, such as the one described in the next section.

2.3 The Galerkin/least-squares formulation

Originally introduced by Hughes and Johnson, the Galerkin/least-squares (GLS) formulation is a full space-time finite element technique employing the discontinuous Galerkin method in time (see [2, 17]). The least-squares operator ensures good stability characteristics while retaining a high level of accuracy. The local control of the solution in the vicinity of sharp gradients is further enhanced by the use of a nonlinear discontinuity-capturing operator.

Let Ω be the spatial domain of interest and Γ its boundary. The semi-discrete Galerkin/least-squares variational problem can be stated as:

Find $\boldsymbol{V}^h \in \mathcal{S}^h$ (trial function space), such that for all $\boldsymbol{W}^h \in \mathcal{V}^h$ (weighting function space), the following equation holds:

$$\begin{aligned} \int_\Omega \Big(W^h \cdot \boldsymbol{U}_{,t}(\boldsymbol{V}^h) \quad &- \quad \boldsymbol{W}^h_{,i} \cdot \boldsymbol{F}^{\mathrm{adv}}_i(\boldsymbol{V}^h) + \boldsymbol{W}^h_{,i} \cdot \widetilde{\boldsymbol{K}}_{ij} \boldsymbol{V}^h_{,j} \Big) \, d\Omega \\ &+ \quad \sum_{e=1}^{n_{\mathrm{el}}} \int_{\Omega^e} \Big(\mathcal{L}\boldsymbol{W}^h \Big) \cdot \boldsymbol{\tau} \Big(\mathcal{L}\boldsymbol{V}^h \Big) \, d\Omega \\ &+ \quad \sum_{e=1}^{n_{\mathrm{el}}} \int_{\Omega^e} \nu^h g^{ij} \boldsymbol{W}^h_{,i} \cdot \widetilde{\boldsymbol{A}}_0 \boldsymbol{V}^h_{,j} \, d\Omega \end{aligned}$$

$$= \int_\Gamma \boldsymbol{W}^h \cdot \Big(- \boldsymbol{F}_i^{\text{adv}}(\boldsymbol{V}^h) + \boldsymbol{F}_i^{\text{diff}}(\boldsymbol{V}^h)\Big) n_i \, d\Gamma. \tag{4}$$

The first and last integrals of (4) represent the Galerkin formulation written in integrated-by-parts form to ensure conservation under reduced quadrature integration.

The second integral constitutes the least-squares operator where $\mathcal{L}$ is defined as

$$\mathcal{L} = \widetilde{\boldsymbol{A}}_0 \frac{\partial}{\partial t} + \widetilde{\boldsymbol{A}}_i \frac{\partial}{\partial x_i} - \frac{\partial}{\partial x_i}(\widetilde{\boldsymbol{K}}_{ij} \frac{\partial}{\partial x_j}). \tag{5}$$

$\boldsymbol{\tau}$ is a symmetric time-scale matrix for which definitions can be found in [17].

The third integral is the nonlinear discontinuity-capturing operator, which is designed to control oscillations about discontinuities, without upsetting higher-order accuracy in smooth regions. g^{ij} is the contravariant metric tensor defined by

$$[g^{ij}] = [\boldsymbol{\xi}_{,i} \cdot \boldsymbol{\xi}_{,j}]^{-1}$$

where $\boldsymbol{\xi} = \boldsymbol{\xi}(\boldsymbol{x})$ is the inverse isoparametric element mapping and ν^h is a scalar-valued homogeneous function of the residual $\mathcal{L}\boldsymbol{V}^h$. The discontinuity capturing factor ν^h used for linear elements is an extension of that introduced by Hughes, Mallet, and Shakib (see [15, 17]).

A key ingredient to the formulation is its consistency: the exact solution of (1) satisfies the variational formulation (4). This constitutes an essential property in order to attain higher-order spatial convergence.

2.4 Extension to higher-order elements

In principle everything is contained in the weighted residual given by Eq. (4). There is no new term to code, no interpolation technique specific to higher order to derive: everything is already there. We just have to compute the integrals of (4), taking into account the new higher-order shape functions.

The volume and surface integrals are numerically evaluated with quadrature rules. All is needed is the values of the shape functions (and their gradients) at the integration points. Higher-order functions only require more precise integration rules. In 2-D, we use 3-, 6-, and 12-point rules, respectively for linear, quadratic, and cubic triangles. They have orders of accuracy which integrate exactly polynomials of degrees 2, 4, and 6 respectively.

For a given number of degrees of freedom, higher-order meshes contain much fewer elements than P1 meshes. In 2-D the ratio is 1/4th for quadratic triangles, and 1/9th for cubic. Although more integration points are required, the higher-order computation of (4) is actually cheaper. The extra cost comes from the implicit linear system which possesses a much larger bandwidth. For a regular 2-D mesh with six triangles connected to a given node, each line of the implicit matrix contains 7, 19, and 37 non-zero blocks, respectively for P1, P2, and P3 elements (for vertex degrees of freedom).

Preliminary quadratic and cubic element results obtained with the original stabilization and discontinuity capturing term used for linear elements, appeared too diffusive especially for inviscid transonic test cases. This is an indication that the intrinsic time scale matrix $\boldsymbol{\tau}$ must be reduced for higher-order elements. Theoretical study of the 1-D scalar advection diffusion equation showed that the optimal $\boldsymbol{\tau}$ must indeed be reduced in the advective limit for any higher-order element. The shock capturing operator must also be tuned in a similar fashion.

In fact, one term in the weighted residual must be specially treated in the context of higher-order elements for the Navier-Stokes equations. The last term in (5) vanishes to zero for linear elements. It appears in the second integral of (4). This term must be computed with higher-degree shape and test functions in order to preserve consistency. In practice, it is evaluated using an L_2-projection.

One-dimensional studies showed that there was no significant differences between SUPG and Galerkin/least-squares. We have chosen to concentrate solely on SUPG which is easier to implement.

As a final remark, we want to stress the fact that whatever the order of the elements, all operations remain local (viz. at the element level). Consequently higher-order elements engender no implicitation nor parallelization issue (see [7]).

2.5 Isoparametric meshes with curved boundaries

We have made the seemingly obvious choice of higher-order **isoparametric** elements. One of the advantages of these elements, besides the higher-order shape functions, is the use of higher-order polynomials to represent curved boundaries. They only ensure C^0 continuity across elements, but locate all the nodes on the actual surface.

We had thought at first that the slope discontinuity across element boundaries could be minimized by adjusting the location of the extra nodes along the sides and the faces of elements beyond P1. In practice it is very easy to generate negative elements with "shamrock"-like edges if one tries to play with node location along edges to optimize curvature. Consequently we sticked in this study to elements with equally distributed nodes along the edges and faces.

All higher-order meshes were obtained by adding nodes to a coarse initial P1 mesh. For more detailed information about higher-order mesh generation, the reader is referred to [12].

3 TWO-DIMENSIONAL VALIDATION TEST CASES

Dassault Aviation computed four of the Mandatory Test Cases (referred to as MTC's) defined in the ADIGMA Project (see [18]). They cover a wide range of applications: from inviscid subsonic and transonic flows (MTC's 1 and 2), to laminar Navier-Stokes (MTC 3), and finally a profile in transonic turbulent conditions (MTC 5). All four test cases were run with the baseline second-order version of Dassault Aviation's industrial

Navier-Stokes code AETHER and with the present work third and fourth order extensions.

3.1 MTC 1: NACA0012, $M = 0.50$, $\alpha = 2°$, inviscid

Higher-order meshes for both inviscid test cases were obtained by adding nodes to a coarse 1106-node P1 mesh. This yields a 4336-node P2 mesh and a 9690-node P3 mesh. Four finer quadratic grids (up to 1,088,896 nodes) and two finer cubic grids (up to 775,386 nodes) were generated. All new nodes are added on the actual profile. This produces boundary elements with curved edges. Elements with no face along the boundary have straight edges.

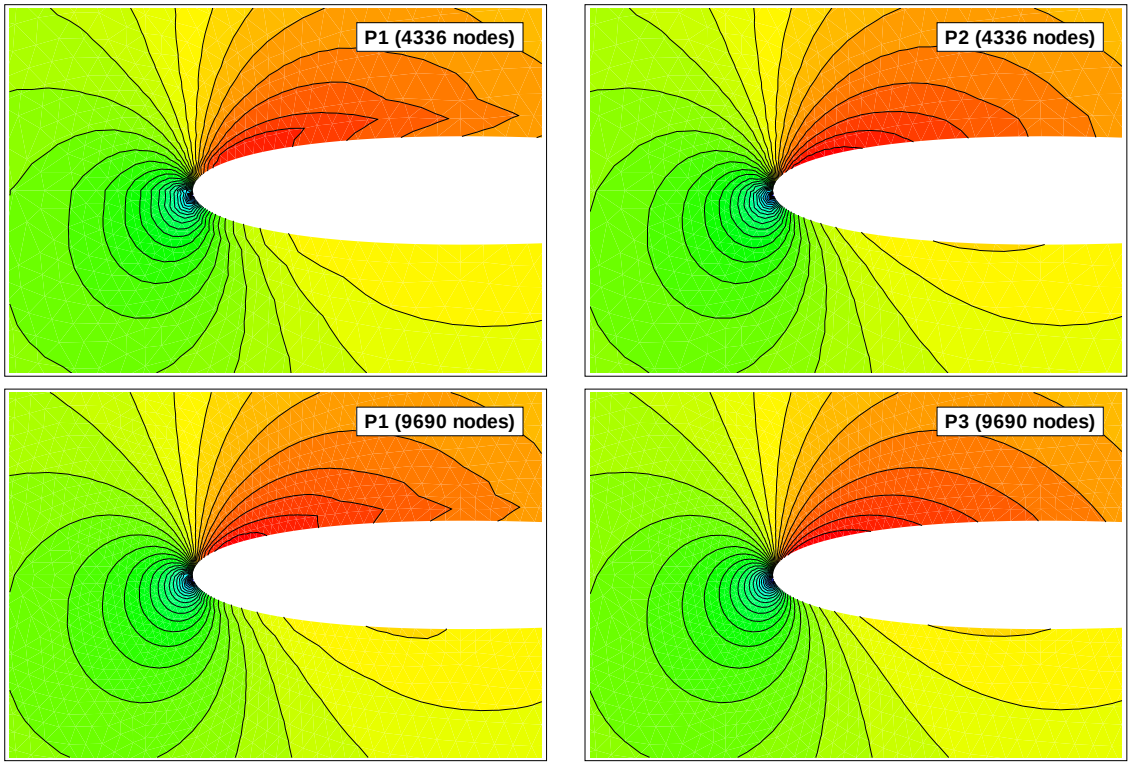

Figure 2: MTC 1: NACA0012, $M = 0.50$, $\alpha = 2°$, inviscid. Mach number contours on matching P1 iso-P2 and P2 grids, and P1 iso-P3 and P3 grids.

Higher-order MTC 1 results are compared with those obtained on the corresponding P1 mesh with the same number of nodes in Figure 2. They clearly show the advantage of the increased order of accuracy brought by quadratic and cubic elements. The entropy layer generated at the stagnation point is much reduced with quadratic elements and virtually disappears with cubic elements. This directly impacts the Mach number contours which traditionally present kinks near the wall on coarse P1 meshes. These kinks are removed from higher-order calculations, which also present much cleaner contours for the same

number of degrees of freedom.

The kinks in Mach number contours observed in second-order solutions along the profile are not due to a lower degree of accuracy boundary condition or boundary integral computation as may have been suggested, but in fact to the level of spurious entropy generated at the leading edge. It is convected along the profile and affects the solution close to the airfoil. This fact is confirmed in [13], where local mesh refinement in the sole leading edge region suppresses the spurious entropy production.

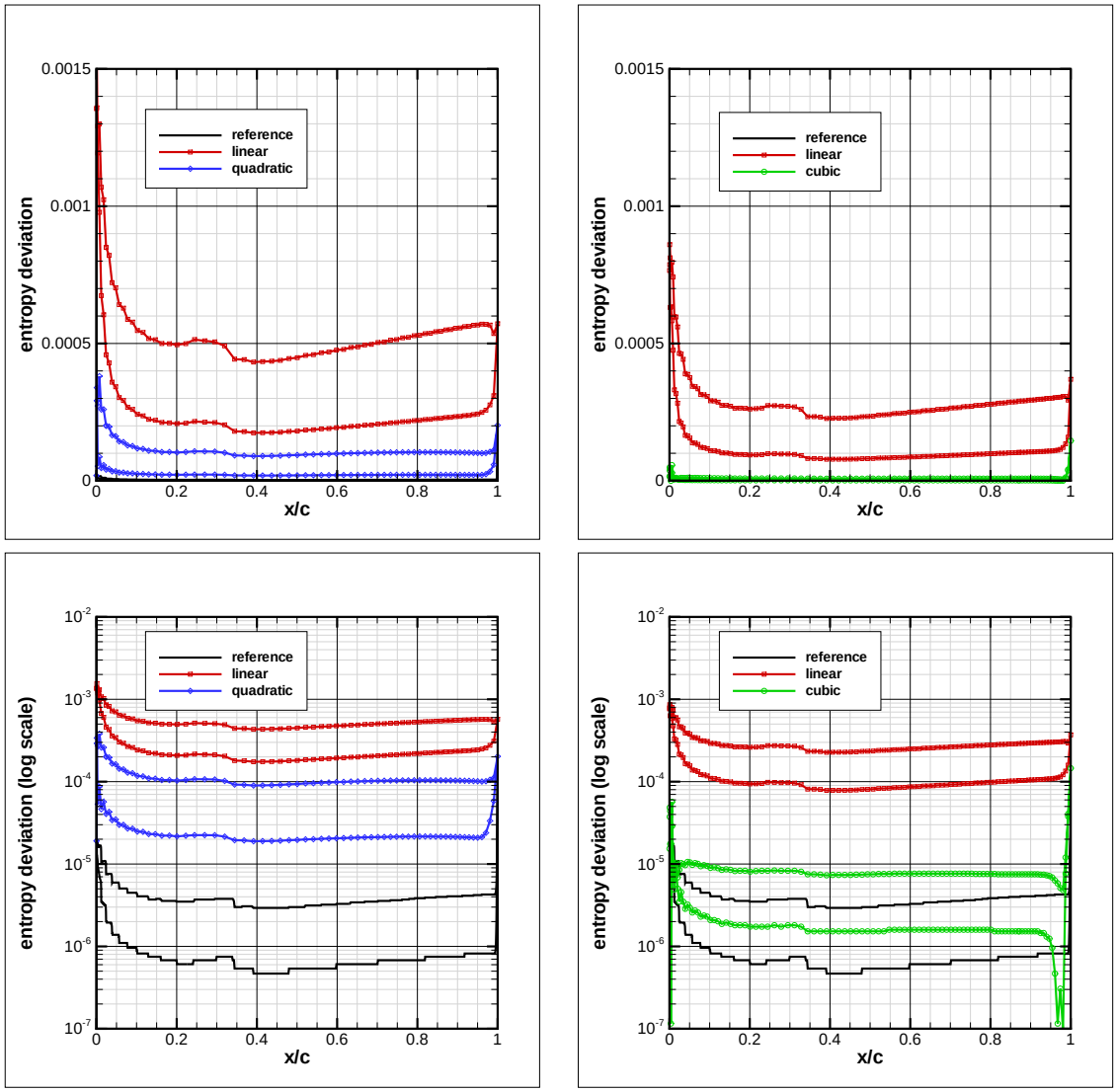

Figure 3: MTC 1: NACA0012, $M = 0.50$, $\alpha = 2°$, inviscid. Line plots of entropy deviation along the profile. Comparison of P1 vs P2, and P1 vs P3 results for the same numbers of degrees of freedom.

Figure 3 displays line plots of entropy deviation along the profile, comparing the baseline linear-element formulation with quadratic and cubic results obtained with the same number of degrees of freedom. The reference P1 calculation was calculated on the finest 1,088,896-node mesh

Entropy line plots show that the spurious entropy layer generated at the stagnation point is much reduced with quadratic elements and virtually disappears with cubic elements. Much finer P1 meshes are required to match the low level of entropy deviation observed with P2 and P3 elements.

Figure 4 presents the convergence of the drag and lift coefficients with respect to the grid size given by its node number or "number of degrees of freedom per equation." The error bars represent the convergence definitions provided for the test case: when a given coefficient reaches within the error bars, the solution is assumed converged for that particular coefficient.

We can notice a dramatic increase in convergence rate with the order of the scheme. Lift is converged for every tested higher-order mesh; drag requires more effort, and may still gain from an increase in scheme order beyond 4. Even CPU time shows a gain with scheme order.

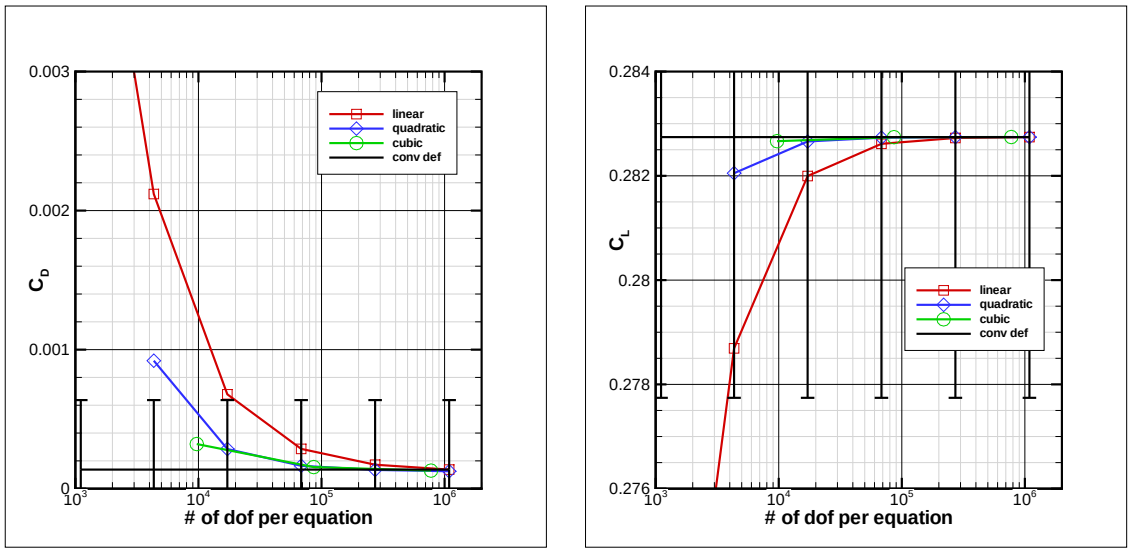

Figure 4: MTC 1: NACA0012, $M = 0.50$, $\alpha = 2°$, inviscid. Convergence of force coefficients for P1, P2, and P3 elements.

3.2 MTC 2: NACA0012, $M = 0.80$, $\alpha = 1.25°$, inviscid

MTC 2 is a transonic inviscid test case. It is interesting in its own respect, since it can challenge the ability of higher-order elements to treat shocks with the help of the discontinuity capturing operator.

Figure 5 shows Mach number contours on the same set of meshes used for MTC 1. In spite of the presence of the shock wave, no obvious degradation in the solution quality can be observed. P3 elements even produce the best result with a well resolved slip line and a finely captured windward-side weak shock.

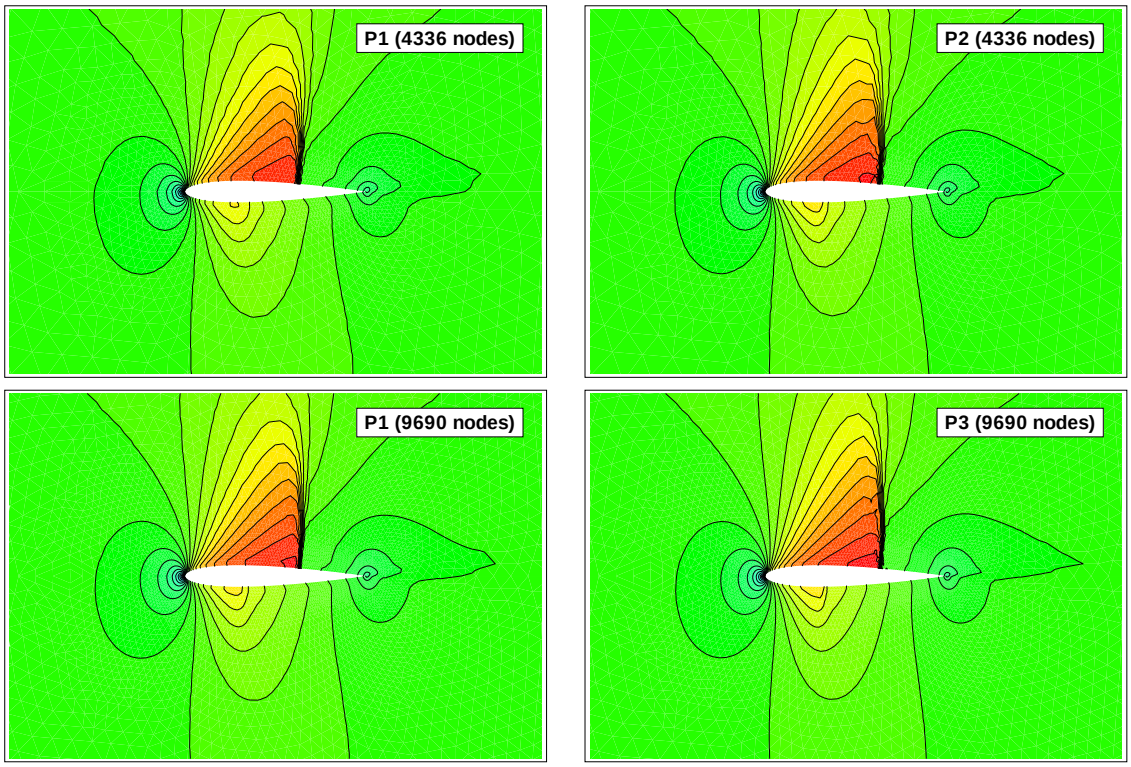

Figure 5: MTC 2: NACA0012, $M = 0.80$, $\alpha = 1.25°$, inviscid. Mach number contours on matching P1 iso-P2 and P2 grids, and P1 iso-P3 and P3 grids.

The pressure line plots shown in Figure 6 display smooth behaviors with sharp shocks, actually sharper than corresponding second order solutions. The windward side weak shock is more accurately captured. The reference solution is that obtained in the asymptotic convergence study with the finest P1 mesh containing 1,088,896 nodes. It must be noted that these line plots do not represent the actual higher-order shape functions within each higher-order element; a linear variation between nodes is assumed.

The spurious entropy layer generated at the stagnation point is again much reduced with quadratic elements and even more so with cubic elements. The levels are not as low

as those obtained for the previous subsonic test case; this is probably due to the presence of the Discontinuity Capturing operator. What is very striking is the accuracy of the entropy rise through the shock wave obtained with higher-order elements: the entropy level after the shock closely matches the reference level obtained on a mesh containing over one million nodes.

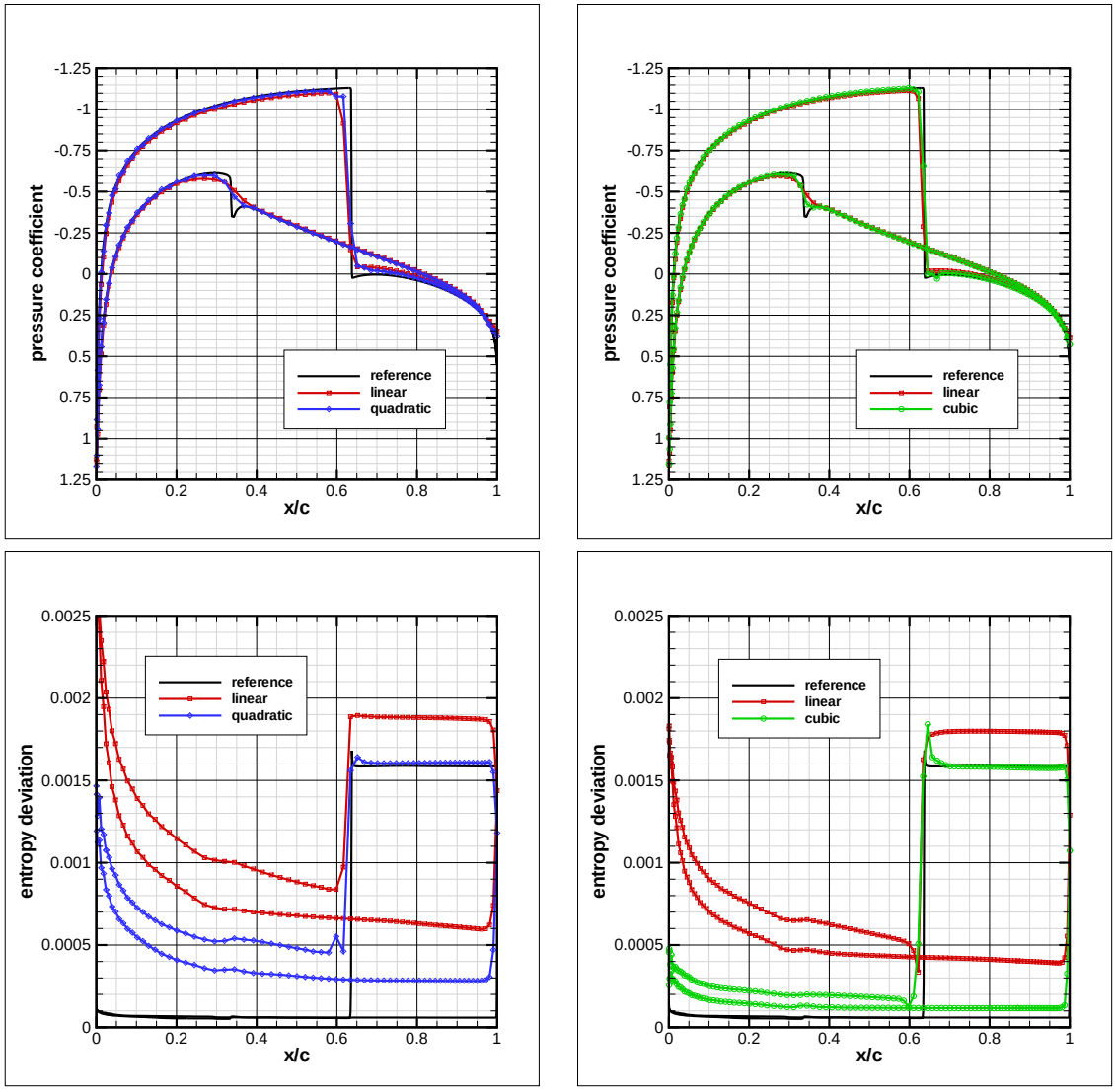

Figure 6: MTC 2: NACA0012, $M = 0.80$, $\alpha = 1.25°$, inviscid. Line plots of pressure coefficient and entropy deviation along the profile. Comparison of P1 vs P2, and P1 vs P3 results for the same numbers of degrees of freedom.

Figure 7 presents the convergence of the drag and lift coefficients. As with MTC 1, all higher-order meshes display a converged lift coefficient, whereas drag requires more mesh

points. Most of the gain is obtained with third order elements. On the average, CPU time to convergence is reduced by 80%.

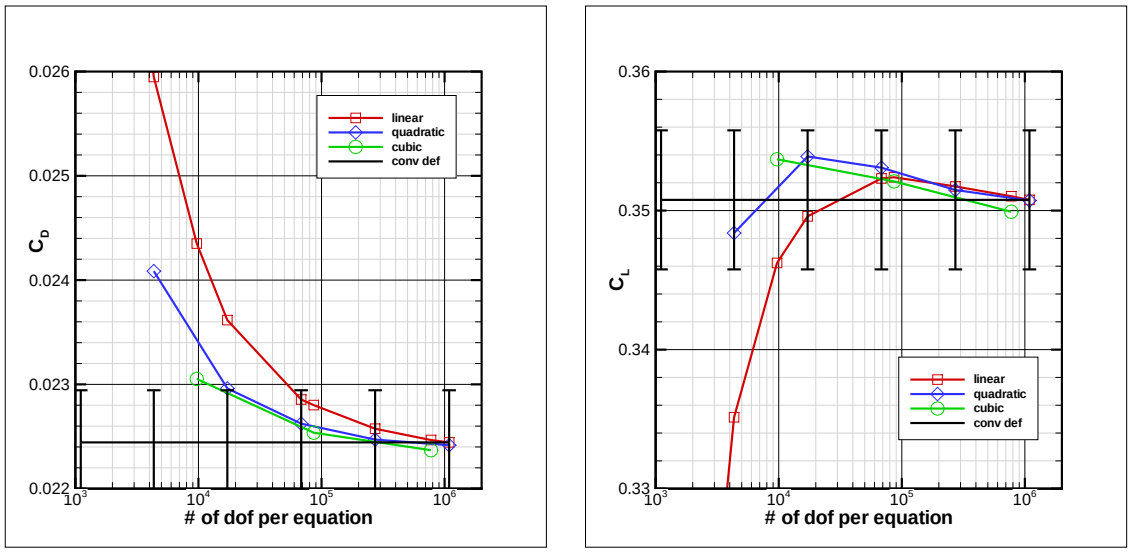

Figure 7: MTC 2: NACA0012, $M = 0.80$, $\alpha = 1.25°$, inviscid. Convergence of force coefficients for P1, P2, and P3 elements.

3.3 MTC 3: NACA0012, $M = 0.50$, $\alpha = 2°$, $Re = 5,000$

We now come to MTC 3, one of the most interesting test cases in the selection. It concerns the laminar computation of an airfoil. Although a Navier-Stokes test case, it is still far from concrete industrial applications. We will see however that it exemplifies the difficulty of getting converged Navier-Stokes solutions. One can anticipate an even greater challenge with complex 3-D RANS computations...

Navier-Stokes meshes with their stretched elements along the boundary bring a specific difficulty: extra nodes added along the boundary may produce negative elements. An initial coarse 1533-node mesh is the starting point of all grids generated for MTC 3. The first P2 and P3 grids contain respectively 6034 and 13,503 nodes. Four finer quadratic grids (up to 1,521,184 nodes) and two finer cubic grids (up to 1,083,159 nodes) were generated.

A mesh deformation technique based on linear elasticity was used to generate stretched and curved higher-order elements close to the airfoil boundary for the Navier-Stokes cases. Unlike the meshes built for the inviscid test cases, these meshes contains elements with curved faces in the volume away from the airfoil surface.

Figure 8 presents pressure contours obtained on the coarsest quadratic and cubic meshes. They are compared with results computed on corresponding linear meshes containing the very same numbers of grid points. P1 results show the difficulty of preserving a

constant pressure through an underresolved boundary layer and highly stretched elements. This difficulty is alleviated with the increasing order of the elements.

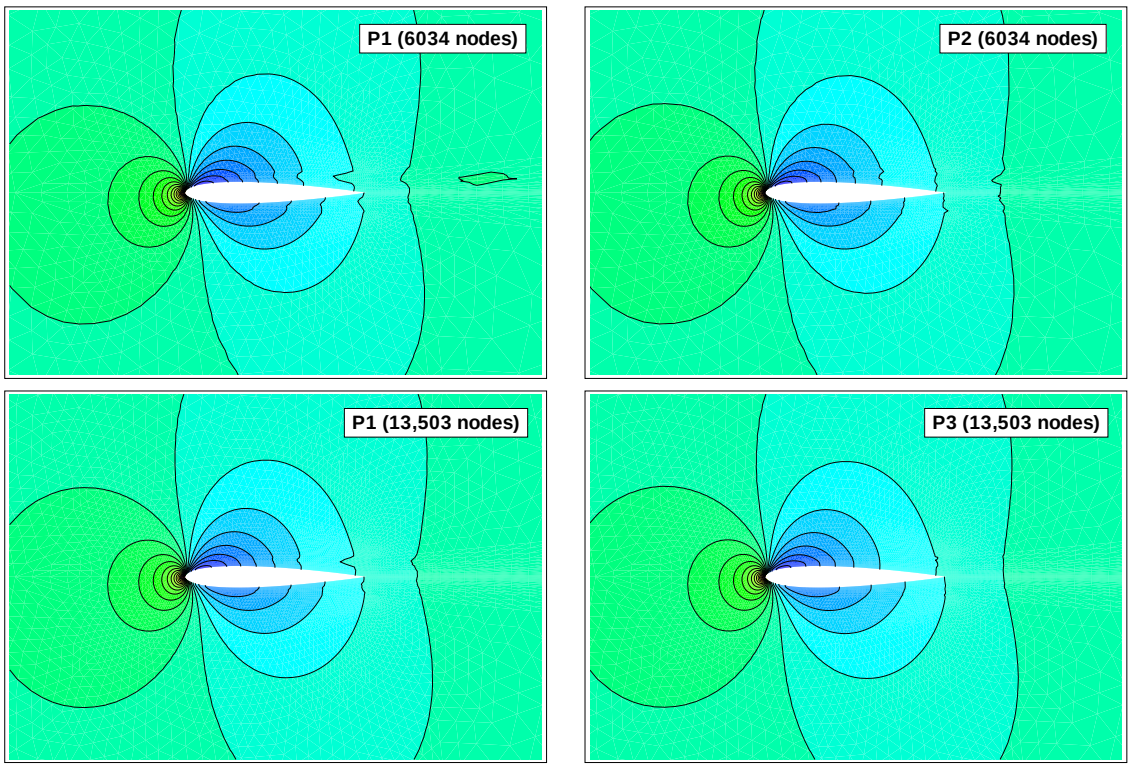

Figure 8: MTC 3: NACA0012, $M = 0.50$, $\alpha = 2°$, $Re = 5,000$. Pressure contours on matching P1 iso-P2 and P2 grids, and P1 iso-P3 and P3 grids.

Figure 9 presents the convergence of force coefficients: pressure drag and lift, friction drag, and heat flux. The advantage of higher-order elements is even more blatant than for the inviscid test cases described previously. Pressure drag and lift converge faster with quadratic elements; cubic elements yield values close to the asymptotic limit for every computed grid, even the coarser ones.

Unexpectedly viscous fluxes appear as a real challenge for this laminar test case. Second order viscous drag is still not converged for the finest mesh which contains over 1.5 million nodes: the asymptotic value is provided by the quadratic results. The magnified plot is even more striking: linear elements have a hard time getting within one drag count of the asymptotic value of the friction drag, whereas as all higher-order results are within half of the same margin. Heat flux convergence plotted in log scale shows the substantial advantage of higher-order elements. The error in heat flux (which should be zero for an adiabatic wall condition) can be reduced by several orders of magnitude.

The number of nodes and the CPU time for convergence are again reduced with the

order of the scheme used. Quadratic elements bring most of the reduction, except for lift which seems to converge at a slower rate and may benefit from an element order beyond 3.

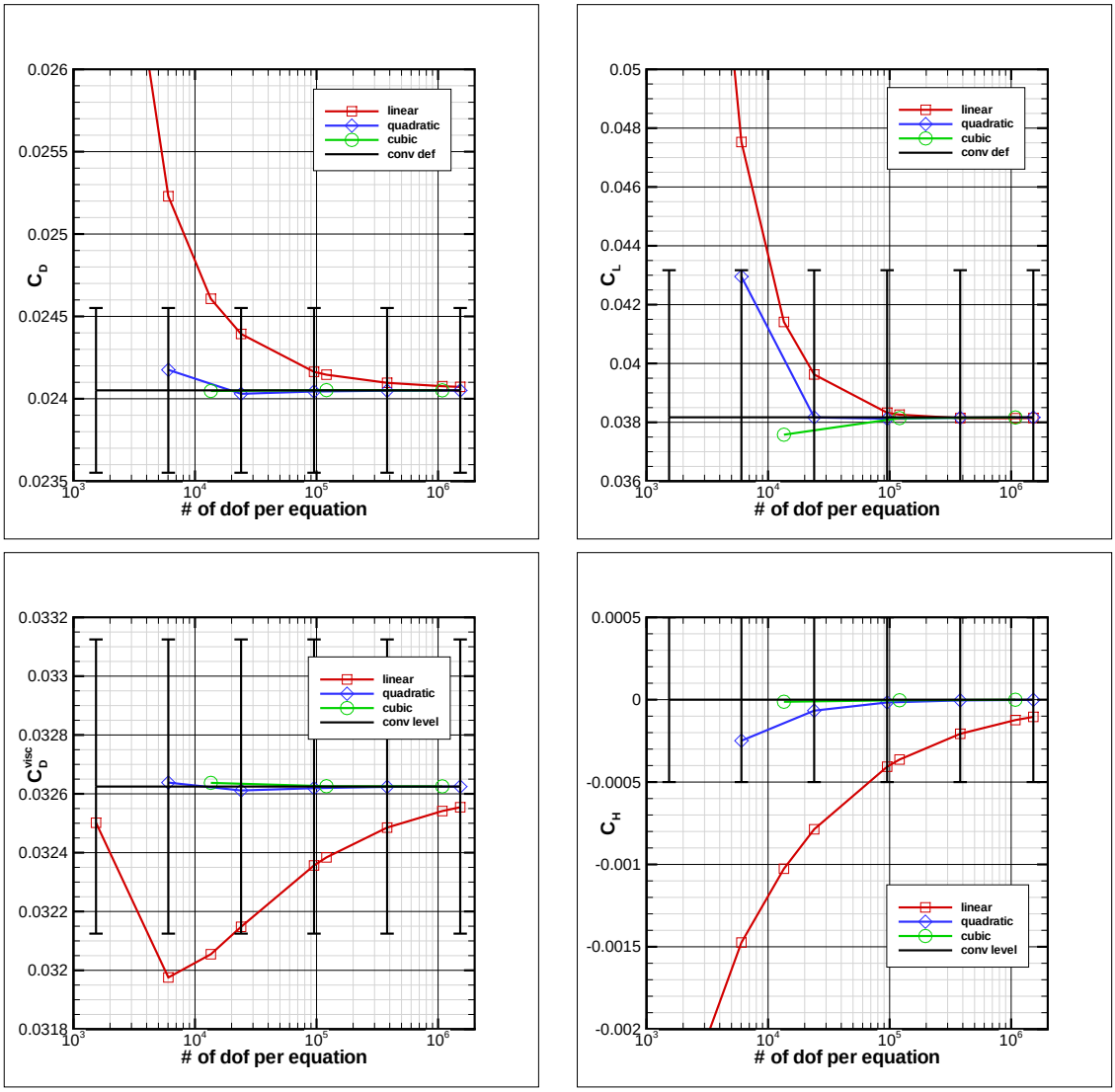

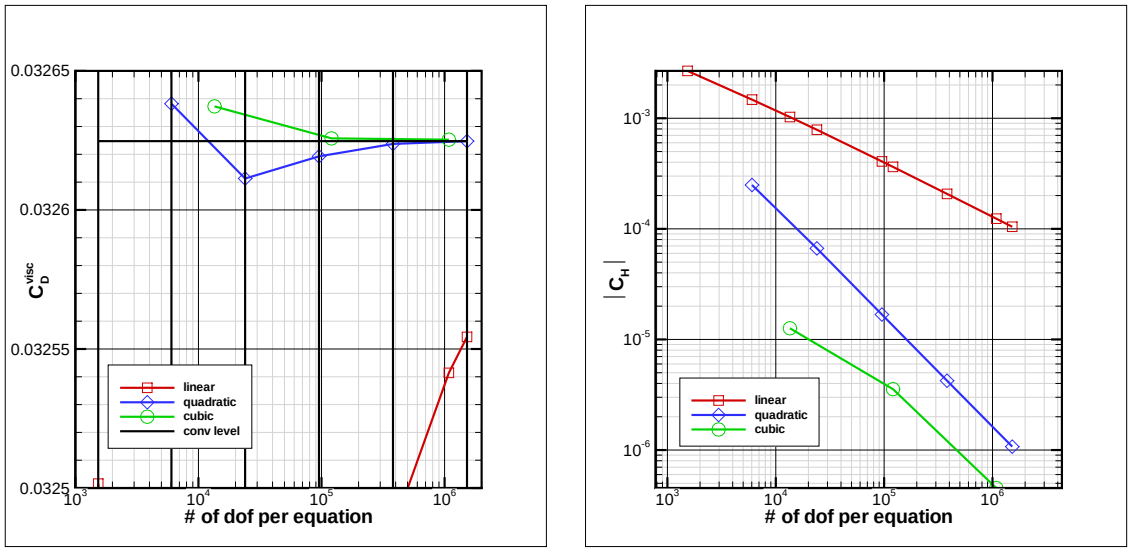

Figure 9: MTC 3: NACA0012, $M = 0.50$, $\alpha = 2°$, $Re = 5,000$. Convergence of force and heat flux coefficients for P1, P2, and P3 elements.

Regarding CPU cost and memory requirements, we can be more specific for this particular test case. For the same number of degrees of freedom, the extra cost of P2 elements over P1 is only 30%; P3 elements are 2 to 2.5 times as expensive as P1 elements. The overhead due to the L_2 projection can however be reduced. The rise in CPU cost is overtaken by the drastic reduction in the number of nodes required for convergence. Consequently the CPU time for convergence decreases with the degree of the scheme. Memory requirements are mostly consumed by the implicit Jacobian matrix. Compared with linear elements, they increase by 30% and 70% respectively for quadratic and cubic elements

3.4 MTC 5: RAE2822, $M = 0.734$, $\alpha = 2.79°$, $Re = 6,500,000$

The final test case deals with a transonic high Reynolds number RANS problem.

A series of P1, P2, and P3 meshes was also generated for MTC 5. The same mesh deformation technique used for MTC 3 grids was applied to obtain stretched and curved higher-order elements close to the airfoil boundary. Highly stretched elements are present close to the airfoil surface and in the wake with aspect ratios up to 2×10^6!

In the numerical method described in Section 2.1, the turbulence equations are solved in a staggered manner, with a second-order residual distribution scheme, and are weakly coupled to the Navier-Stokes field through the turbulent viscosity μ_t.

As a first step, for higher-order calculations, RANS turbulent equations are solved on an underlying P1 mesh, and thus remain second-order accurate. These first results show the robustness of the SUPG finite element method. As for the more elementary MTC's (1, 2, and 3), the convergence of quadratic and cubic elements is similar to that obtained

for linear elements with the same CFL settings. High aspect ratios do not seem to be an issue.

Figure 10 presents Mach number contours obtained with P1, P2, and P3 elements on matching grids. On these fairly coarse meshes, it's hard to see any difference between the solutions.

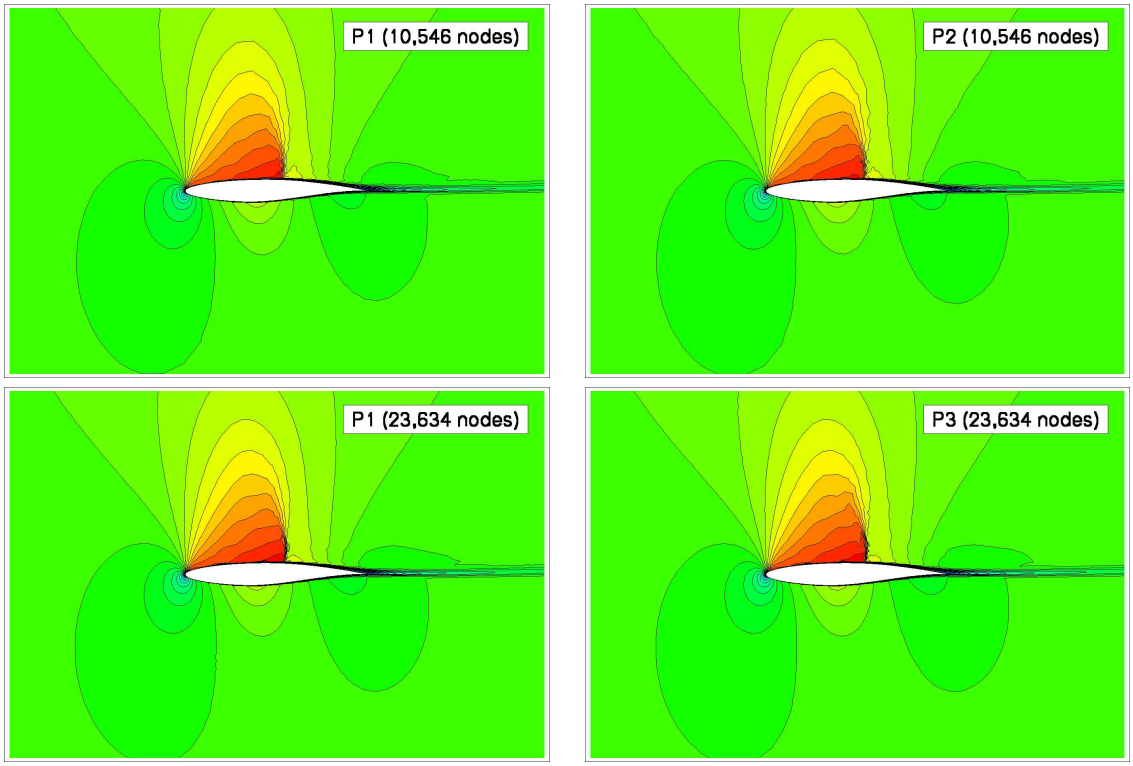

Figure 10: MTC 5: RAE2822, $M = 0.734$, $\alpha = 2.79°$, $Re = 6,500,000$. Mach number contours on matching P1 iso-P2 and P2 grids, and P1 iso-P3 and P3 grids.

The force coefficient convergence plots are gathered in Figure 11. The open symbol curves represent the second-, third-, and fourth-order methods described above (with a second order turbulence model). There is no real distinction between the three schemes. They converge at the same rate toward the same asymptotic values. Nevertheless heat flux shows once more an indisputable advantage of higher-order elements over linear ones. The error is smaller by as much as three orders of magnitude. There is no additional benefit brought by cubic elements though.

In an attempt to simulate a "higher-order" turbulence model, we used the interpolation of the μ_t field computed on the finest P1 mesh (2,669,536 nodes). The outcome of this test is indicated in the different convergence plots of Fig. 11 with filled symbols. We have only tested linear and quadratic elements. Results show that the turbulence model has a huge impact on the convergence of force coefficients. Quadratic elements have a

slight edge over linear elements, especially for the coarsest meshes. Heat flux convergence is unaffected. This demonstrates the need for a higher-order turbulence model to fully exploit in RANS computations the benefit of higher-order elements observed in inviscid and laminar test cases.

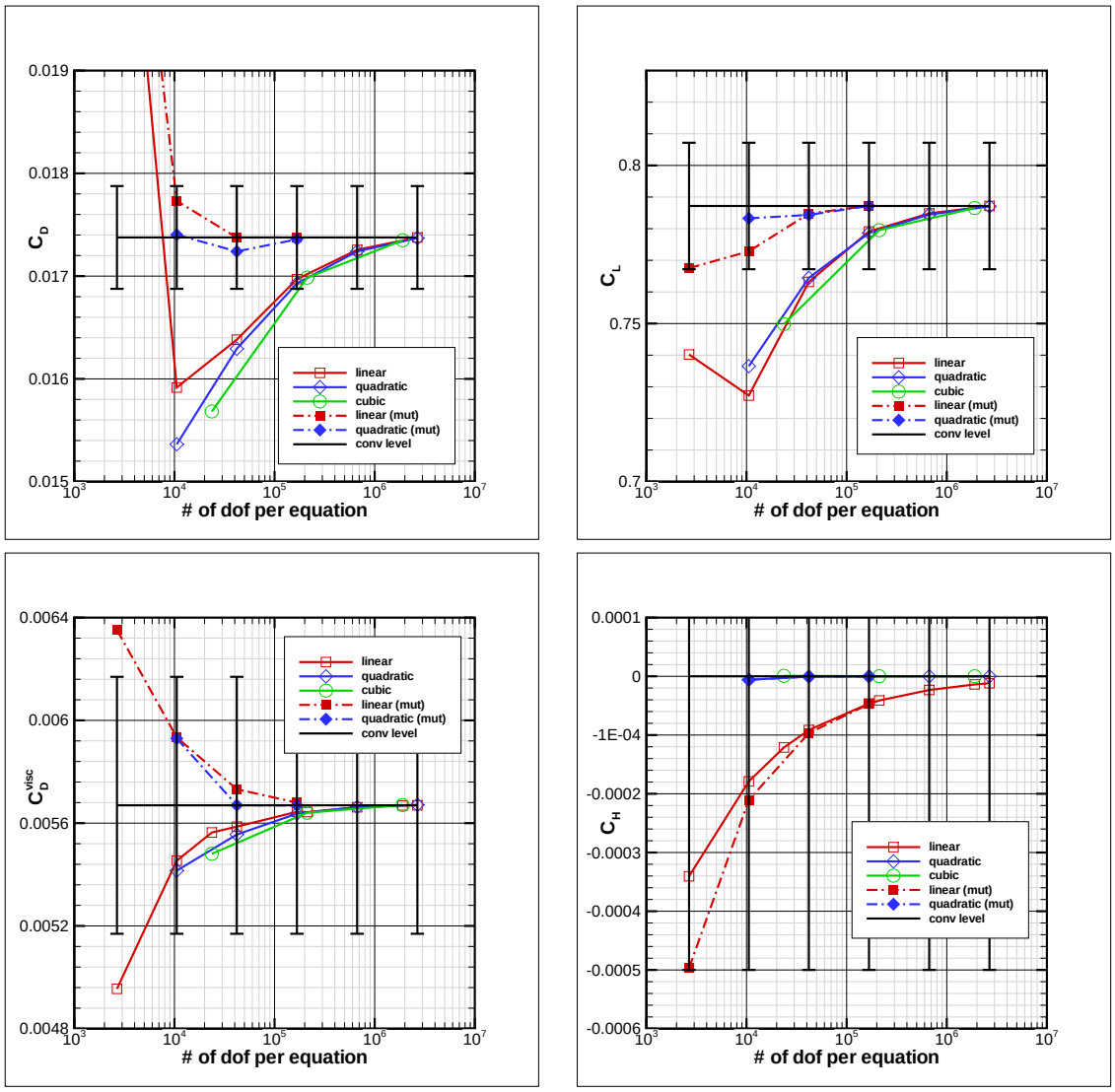

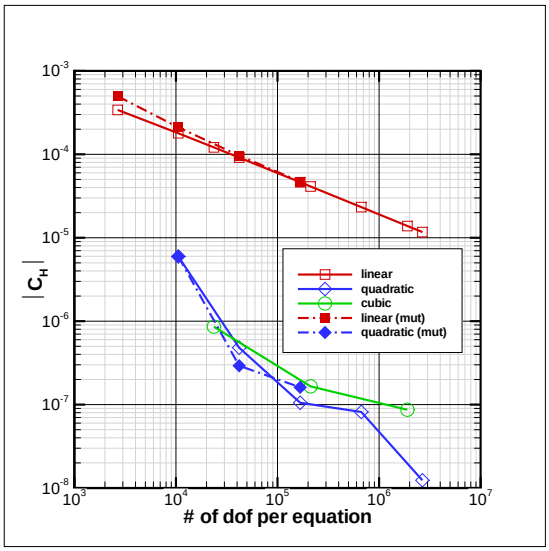

Figure 11: MTC 5: RAE2822, $M = 0.734$, $\alpha = 2.79°$, $Re = 6,500,000$. Convergence of force and heat flux coefficients for P1, P2, and P3 elements.

4 TOWARDS INDUSTRIAL APPLICATIONS: A FIRST HIGHER-ORDER FULL AIRCRAFT COMPUTATION

After the gradual and careful 2-D testing of quadratic and cubic triangular elements for different flow conditions, the higher-order three-dimensional capability of the code was checked on simple test cases such as an inviscid subsonic sphere (which showed drag vanish with the increased order of the elements) and the ONERA M6 wing (both inviscid and laminar). Higher-order quadratic and cubic tetrahedral meshes were obtained by enriching a reference P1 mesh in a fashion similar to what was done in two dimensions.

Unfortunately the systematic asymptotic convergence analysis performed for 2-D test cases is just not feasible even for these simple 3-D geometries: meshes would exceed very quickly hundreds of millions nodes. A dedicated way to generate higher-order meshes from scratch is really needed.

In the mean time, since all the ingredients are here, it feels nonetheless very tempting to test a real 3-D industrial geometry. What is missing is a higher-order 3-D mesh. We looked for the coarsest full aircraft mesh available. We found a Falcon 900EX design mesh from a few years back, complete with vertical tail and empennage, pylons, nacelles and S-duct. It contains "only" 2,512,073 nodes. A cut through this mesh downstream of the wings, at the level of the engines is presented in Figure 12 in blue. One must note that this mesh is not adjusted for drag prediction with heavy refinement in the wake regions.

We built two grids based on this reference mesh: one linear P1 iso-P2 grid, and one quadratic P2 grid both containing 19,905,887 nodes. A cut through the linear refined

tetrahedral mesh can be see in red in Figure 12.

The exercise has a few limitations. First the additional body nodes were not projected on the actual surface of the aircraft: all the elements have straight edges and sub-parametric coordinate transformations are used (although everything is coded with isoparametric transformations). As described in section 3.4, all computations were performed using a second-order scheme for the turbulence equations. Only quadratic elements were tested and on a single mesh size.

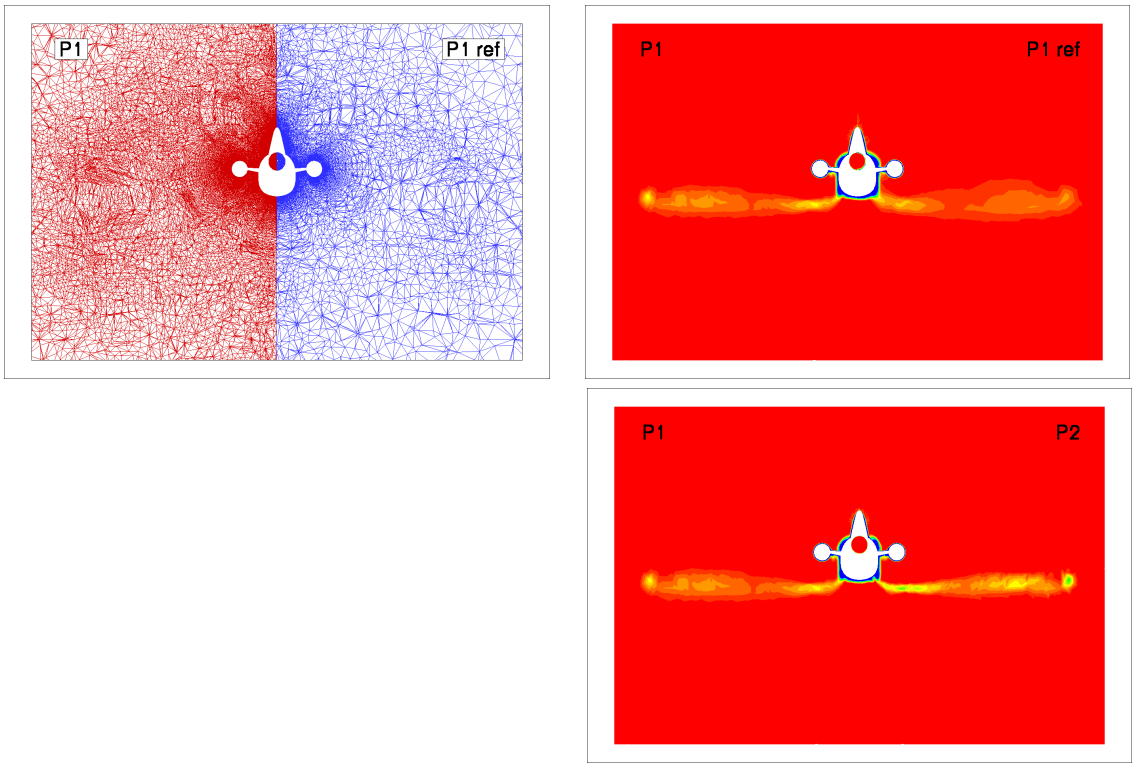

Figure 12: Falcon 900EX: $M = 0.80$, $\alpha = 2.0°$, $Re = 14,500,000$. Clockwise from top left: cut through original 2,512,073-node P1 mesh (right) and corresponding uniformly refined 19,905,887-node P1 iso-P2 mesh (left); entropy contours for the original P1 mesh (right) and the uniformly refined P1 iso-P2 mesh (left); entropy contours for the P2 mesh (right) and the uniformly refined P1 iso-P2 mesh (left).

We used respectively a 1-point integration rule for linear tetrahedra and an 8-point rule for quadratic ones. The ratio between the number of elements of a P1 and a P2 tetrahedron mesh with the same number of nodes is 8. Consequently in principle the cost of a residual evaluation should be similar on the P1 and P2 meshes. Due to the higher-order coupling between degrees of freedom, the implicit Jacobian is roughly twice as big for P2 elements. This yields an extra cost when generating the operator and during the actual linear solve. Globally, the third-order computation is 68% more expensive than the second-order one, using the same CFL setting. This could be reduced for instance if

the implicit operator is not updated at each time step or if the original P1 matrix is used (possibly at the cost of reduced robustness). The memory requirement is increased by 61%. Convergence is similar between P1 and P2 calculations with the same CFL settings. Computations were done in parallel on an IBM Blue Gene/P using 1024 tasks.

Figure 12 presents entropy contours in vertical cuts through the aft part of the aircraft, in the engine region, downstream of the wing. The wake of the wing is slightly more defined in the 20-million-node P1 mesh in comparison with the original 2.5-million-node mesh. The third order result displays a much more detailed wake and a stronger tip vortex. This is also exemplified in Figure 1 which shows a more persistent and stronger wake in the quadratic element result.

It is common to see discrepancies between near-field and far-field drag analyses (see [14, 19]). The difference between these two drag evaluations is known as "spurious drag." In the reference 2.5-million-node P1 computation, the spurious drag amounts to 33 drag counts (10^{-4}). With the uniformly refined 20-million-node P1 mesh, it drops to 8 counts which is pretty good. Drag analysis performed on the third-order solution (with standard linear tools) indicates that the spurious drag is further reduced to just 1 count! This preliminary drag analysis suggests that spurious drag virtually disappears with increased order of accuracy.

5 CONCLUDING REMARKS

In this study, we have achieved:

- the implementation of higher-order (quadratic and cubic) stabilized finite elements for compressible flows in an industrial code;
- the systematic convergence study of increasingly difficult test cases: inviscid, transonic, laminar, and turbulent flows;
- the proof that higher-order convergence can be achieved at a reasonable cost;
- the demonstration that higher-order elements are robust: same CFL rules where applied in our simulations with convergences similar to linear elements and sometimes significantly better; high aspect ratios can be handled without difficulty;
- the verification that higher-order elements bring no particular complications in terms of implicitation nor parallel efficiency, which is mandatory for industrial applications.

Difficulties were encountered with the RANS test cases. We believe they can be palliated with a stronger higher-order coupling between the Navier-Stokes solver and the turbulence model, or the use of a genuine higher-order scheme for solving the turbulence equations. This is the subject of the PhD thesis of the second co-author. In the mean time, higher-order elements might show a unique potential for Large Eddy Simulations.

As a conclusion, we'll comment on the transition towards industrial applications. The extension to 3-D is readily available and has been successfully tested on a complete aircraft configuration. To make it industrially viable, one needs a dedicated way to generate higher-order meshes. Preliminary drag analysis shows that spurious drag is considerably reduced by the use of higher-order elements.

ACKNOWLEDGEMENTS

This work was supported by the project ADIGMA "Adaptive Higher-Order Variational Methods for Aerodynamic Applications in Industry" funded by the European Community represented by the CEC, Research Directorate-General, in the 6$^{\text{th}}$ Framework Programme, under Contract No. AST5-CT-2006-030719.

Pierre-Elie Normand is supported by a DGA fellowship of the French Ministry of Defense.

REFERENCES

[1] *ADIGMA – A European Initiative on the Development of Adaptive Higher-Order Variational Methods for Aerospace Applications. Results of a collaborative research project funded by the European Union, 2006–2009*, N. Kroll, H. Bieler, H. Deconinck, V. Couallier, H. van der Ven, and K. Sørensen Editors, Notes on Numerical Fluid Mechanics and Multidisciplinary Design, Springer Verlag, to appear.

[2] A.N. Brooks and T.T.R. Hughes, Streamline Upwind Petrov Galerkin formulation for convection dominated flows with particular emphasis on the incompressible Navier-Stokes equations, *Computer Methods in Applied Mechanics and Engineering*, Vol. 32, pp 199–259, 1982.

[3] F. Chalot, T.J.R. Hughes, Z. Johan, and F. Shakib, Application of the Galerkin/least-squares formulation to the analysis of hypersonic flows. I: Flow over a two-dimensional ramp, *Hypersonic Flows for Reentry Problems. Volume II: Test Cases – Experiments and Computations*, Proceedings of a Workshop held in Antibes, France, 22–25 January 1990, Springer Verlag, pp 181–200, 1991.

[4] F. Chalot, T.J.R. Hughes, and F. Shakib, Symmetrization of conservation laws with entropy for high-temperature hypersonic computations, *Computing Systems in Engineering,* vol. 1, pp. 465–521, 1990.

[5] F. Chalot and T.J.R. Hughes, A consistent equilibrium chemistry algorithm for hypersonic flows, *Computer Methods in Applied Mechanics and Engineering,* vol. 112, pp. 25–40, 1994.

[6] F. Chalot, M. Mallet, and M. Ravachol, A comprehensive finite element Navier-Stokes solver for low- and high-speed aircraft design, Paper #94-0814, *AIAA 32nd Aerospace Sciences Meeting,* Reno, NV, January 10–13, 1994.

[7] F. Chalot, Q.V. Dinh, M. Mallet, A. Naïm, and M. Ravachol, A multi-platform shared- or distributed-memory Navier-Stokes code, *Parallel CFD '97,* Manchester, UK, May 19–21, 1997.

[8] F. Chalot, B. Marquez, M. Ravachol, F. Ducros, F. Nicoud, and T. Poinsot, A consistent Finite Element approach to Large Eddy Simulation, Paper #98-2652, *AIAA 29th Fluid Dynamics Conference,* Albuquerque, NM, June 15-18, 1998.

[9] F. Chalot, B. Marquez, M. Ravachol, F. Ducros, and T. Poinsot, Large Eddy Simulation of a compressible mixing layer: study of the mixing enhancement, Paper #99-3358, *AIAA 14th Computational Fluid Dynamics Conference,* Norfolk, VA, June 28-July 1, 1999.

[10] F. Chalot, Industrial aerodynamics, *Encyclopedia of Computational Mechanics*, Vol. 3, Computational Fluid Dynamics, chapter 12, E. Stein, R. de Borst, and T.J.R. Hughes editors, Wiley, 2004.

[11] F. Chalot, V. Levasseur, M. Mallet, G. Petit, and N. Réau, LES and DES simulations for aircraft design, Paper #2007-0723, *45th AIAA Aerospace Sciences Meeting and Exhibit,* Reno, NV, January 8–11, 2007.

[12] F. Chalot and P.-E. Normand, Higher-order Stabilized Finite Elements in an Industrial Navier-Stokes Code, *ADIGMA – A European Initiative on the Development of Adaptive Higher-Order Variational Methods for Aerospace Applications. Results of a collaborative research project funded by the European Union, 2006–2009*, N. Kroll, H. Bieler, H. Deconinck, V. Couallier, H. van der Ven, and K. Sørensen Editors, Notes on Numerical Fluid Mechanics and Multidisciplinary Design, Springer Verlag, to appear.

[13] F. Chalot, Goal-oriented Mesh Adaptation in an Industrial Stabilized Finite Element Navier-Stokes Code *ADIGMA – A European Initiative on the Development of Adaptive Higher-Order Variational Methods for Aerospace Applications. Results of a collaborative research project funded by the European Union, 2006–2009*, N. Kroll, H. Bieler, H. Deconinck, V. Couallier, H. van der Ven, and K. Sørensen Editors, Notes on Numerical Fluid Mechanics and Multidisciplinary Design, Springer Verlag, to appear.

[14] D. Destarac, Far-field/near-field drag balance and applications of drag extraction in CFD, VKI Lecture Series 2003, *CFD-based Aircraft Drag Prediction and Reduction,* National Institute of Aerospace, Hampton, VA, November 3–7, 2003.

[15] T.J.R. Hughes and M. Mallet, A new finite element formulation for computational fluid dynamics: IV A discontinuity-capturing operator for multidimensional advective

- diffusive systems, *Comp. Meth. in Applied Mech. and Eng.,* Vol. 58, pp. 329–336, 1986.

[16] F. Shakib, T.J.R. Hughes, and Z. Johan, A multi-element group preconditioned GMRES algorithm for nonsymmetric systems arising in finite element analysis, *Computer Methods in Applied Mechanics and Engineering,* Vol. 75, pp 415-456, 1989.

[17] F. Shakib, T.J.R. Hughes, and Z. Johan, A new finite element formulation for computational fluid dynamics: X. The compressible Euler and Navier-Stokes equations, *Computer Methods in Applied Mechanics and Engineering,* Vol. 89, pp 141–219, 1991.

[18] K.A. Sørensen and H. Bieler, Verification and assessment, *ADIGMA – A European Initiative on the Development of Adaptive Higher-Order Variational Methods for Aerospace Applications. Results of a collaborative research project funded by the European Union, 2006–2009*, N. Kroll, H. Bieler, H. Deconinck, V. Couallier, H. van der Ven, and K. Sørensen Editors, Notes on Numerical Fluid Mechanics and Multidisciplinary Design, Springer Verlag, to appear.

[19] J. van der Vooren and D. Destarac, Drag/thrust analysis of jet-propelled transonic transport aircraft; definition of physical drag components, *Aerospace Science & Technology,* Vol. 8, pp 545–556, 2004.